Corsica (table S1 and fig. S1). This island's dry northern interior today receives ~30% less precipitation than its margins (fig. S2A), whereas this difference was ~50% during the LGM (fig. S4C). Although this prediction cannot (yet) be confirmed with the data available outside Corsica, it does agree with patterns seen in LGM reconstructions with the high-resolution climate model HadRM (*23*). As mentioned above, locally enhanced precipitation would largely reduce the local lapse rate, so that much of the initially (first-order) inferred temperature anomaly pattern in fact reflects the impact of precipitation anomalies.

Although care must be taken not to simply ascribe past regional property distributions to modern climate oscillation patterns (*24*), it remains useful to consider instrumental records and proxy data in order to develop a sense of realistic analogous climate patterns over the study region (*25*). The contrast between strongly reduced SST in the western basin and much less reduced SST in the central Mediterranean basin during the LGM (Fig. 1) indicates a preferentially meridional geostrophic circulation, with a polar trough that frequently protruded into the western Mediterranean. Such a circulation is favored by northward extension of the Azores High toward Iceland (North Atlantic ridge) or Greenland, blocking moisture supply by the westerlies. It is further enhanced by expansion and intensification of the Siberian High in winter during glacial times (*26*). A similar configuration is thought to have been common during the late Little Ice Age, notably the Maunder Minimum (*2*, *27*). The invasion of polar air as shown by our data, channeled by the topography of mountain ranges and ice sheets in Europe, would have generated cyclone formation in the Gulf of Genoa more frequently than at present, enhancing precipitation along various storm tracks in easterly directions. Our observations do not support a straightforward zonal LGM atmospheric circulation, as inferred from climate models (*19*, *28*). Instead, we propose that frequent meridional circulation during cold seasons (characterized by the LGM ELA pattern) may have alternated with more zonal circulation during warm seasons. A more comprehensive quantitative assessment of the preferential LGM atmospheric circulation requires the use of both nested model simulation and high-resolution global climate model studies (*4*, *5*, *8*, *28*), which should fully resolve the changing topography of glaciated mountain ranges and ice sheets. The validation of such models with our three-dimensional LGM climate proxy data ranging from the sea surface to alpine altitudes is a great future challenge.

References and Notes

1. E. Xoplaki, J. F. Gonzalez-Rouco, J. Luterbacher, H. Wanner, *Clim. Dyn.* **23**, 63 (2004).
2. J. Luterbacher *et al.*, in *The Mediterranean Climate: An Overview of the Main Characteristics and Issues*, P. Lionello, P. Malanotte-Rizzoli, R. Boscolo, Eds. (Elsevier, Amsterdam, 2006), pp. 27–148.
3. COHMAP Members, *Science* **241**, 1043 (1988).
4. M. Kageyama *et al.*, *Quat. Sci. Rev.* **25**, 2082 (2006).
5. G. Ramstein *et al.*, *Clim. Past* **3**, 331 (2007).
6. G. Bond *et al.*, *Nature* **365**, 143 (1993).
7. O. Peyron *et al.*, *Quat. Res.* **49**, 183 (1998).
8. H. Wu, J. Guiot, S. Brewer, Z. Guo, *Clim. Dyn.* **29**, 211 (2007).
9. H. Kerschner, G. Kaser, R. Sailer, *Ann. Glaciol.* **31**, 80 (2000).
10. D. Steiner *et al.*, *Clim. Change,* 10.1007/s10584-008-9393-1 (2008).
11. M. Conkright *et al.*, *World Ocean Atlas 1998 CD ROM Data Set Documentation* (Technical Report 15, NODC Internal Report, Silver Spring, MD, 1998).
12. A. Hayes, M. Kucera, N. Kallel, L. Sbaffi, E. J. Rohling, *Quat. Sci. Rev.* **24**, 999 (2005).
13. A. Paul, C. Schäfer-Neth, *Palaeoceanography* **18**, 1058 (2003).
14. I. Cacho, J. O. Grimalt, M. Canals, *J. Mar. Syst.* **33-34**, 253 (2002).
15. N. Pinardi, E. Masetti, *Palaeogeogr. Palaeoclimatol. Palaeoecol.* **158**, 153 (2000).
16. B. Messerli, *Geogr. Helv.* **22**, 105 (1967).
17. V. Masson-Delmotte *et al.*, *Clim. Dyn.* **26**, 513 (2006).
18. E. J. Rohling, A. Hayes, D. Kroon, S. De Rijk, W. J. Zachariasse, *Palaeoceanography* **13**, 316 (1998).
19. M. Kageyama, F. D. Andrea, G. Ramstein, P. J. Valdes, R. Vautard, *Clim. Dyn.* **15**, 773 (1999).
20. D. Florineth, C. Schlüchter, *Quat. Res.* **54**, 295 (2000).
21. J. C. Larrasoana, A. P. Roberts, E. J. Rohling, M. Winklhofer, R. Wehausen, *Clim. Dyn.* **21**, 689 (2003).
22. U. Pflaumann *et al.*, *Palaeoceanography* **18**, 10.1029/2002PA000774 (2003).
23. A. Jost *et al.*, *Clim. Dyn.* **24**, 577 (2005).
24. F. Justino, W. R. Peltier, *Geophys. Res. Lett.* **32**, 10.1029/2005GL023822 (2005).
25. C. Cassou, L. Terray, J. W. Hurrell, C. Deser, *J. Clim.* **17**, 1055 (2004).
26. E. J. Rohling, P. A. Mayewski, P. Challenor, *Clim. Dyn.* **20**, 257 (2003).
27. J. Jacobeit, P. Jönsson, L. Bärring, C. Beck, M. Ekström, *Clim. Change* **48**, 219 (2001).
28. A. Laîné *et al.*, *Clim. Dyn.,* 10.1007/s00382-008-0391-9 (2008).

29. We gratefully acknowledge funding by the German Science Foundation (DFG project KU1298/7) and the UK Natural Environment Research Council's thematic program Quantifying the Earth System (QUEST).

Supporting Online Material

www.sciencemag.org/cgi/content/full/1157638/DC1
Data Supplements S1 to S3
Figs. S1 to S7
Tables S1 and S2
References

11 March 2008; accepted 21 July 2008
Published online 31 July 2008;
10.1126/science.1157638
Include this information when citing this paper.

Kinematic Constraints on Glacier Contributions to 21st-Century Sea-Level Rise

W. T. Pfeffer,[1]* J. T. Harper,[2] S. O'Neel[3]

On the basis of climate modeling and analogies with past conditions, the potential for multimeter increases in sea level by the end of the 21st century has been proposed. We consider glaciological conditions required for large sea-level rise to occur by 2100 and conclude that increases in excess of 2 meters are physically untenable. We find that a total sea-level rise of about 2 meters by 2100 could occur under physically possible glaciological conditions but only if all variables are quickly accelerated to extremely high limits. More plausible but still accelerated conditions lead to total sea-level rise by 2100 of about 0.8 meter. These roughly constrained scenarios provide a "most likely" starting point for refinements in sea-level forecasts that include ice flow dynamics.

Eustatic land ice contributions to sea-level change come from surface mass balance (SMB) losses and discharge of ice into the ocean through marine-terminating glaciers. Dynamically forced discharge, via fast flow and calving of marine-terminating glaciers allowing rapid land-to-ocean transfer of ice, is well known from studies of temperate marine-terminating glaciers (*1*–*4*) and is observed in Greenland (*5*–*7*). The consensus estimate of sea-level rise (SLR) by 2100 (0.18 to 0.6 m) that was published in the Intergovernmental Panel on Climate Change (IPCC) Fourth Assessment (*8*) excluded dynamic effects on the grounds that present understanding of the relevant processes is too limited for reliable model estimates. Because modeling (*9*) and paleoclimate comparisons (*10*) have yielded multimeter per century estimates of SLR, similar increases have been inferred as a viable 21st-century scenario. Also argued is that feedbacks unaccounted for in the IPCC estimate could quickly cause several meters of very rapid SLR (*11*, *12*).

Accurate SLR forecasts on the century time scale are imperative for planning constructive and cost-effective responses. Underestimates will prompt inadequate preparation for change, whereas overestimates will exhaust and redirect resources inappropriately. Raising California Central Valley levees only 0.15 m, for example, will cost over $1 billion (*13*); the nonlinearly increasing costs of raising levees 2 m or more without clear and compelling cause would entail enormous expenditures otherwise used for different responses as demanded by a smaller but still significant SLR.

We address the plausibility of very rapid SLR from land ice occurring this century. We give

[1]Institute of Arctic and Alpine Research, University of Colorado, Boulder, CO 80309, USA. [2]Department of Geosciences, University of Montana, Missoula, MT 59812, USA. [3]Scripps Institution of Oceanography, University of California San Diego, San Diego, CA 92093, USA.

*To whom correspondence should be addressed. E-mail: pfeffer@tintin.colorado.edu

particular emphasis to Greenland because of its vulnerability to ongoing Arctic warming and meltwater-related feedbacks, recent accelerations of ice motion, and its large volume reductions during the last interglacial (*14*). By using a simple kinematic approach, we determined Greenland and Antarctic outlet glacier velocities required to achieve various magnitudes of SLR by 2100.

To begin, we postulated sea-level increases of 2 and 5 m by 2100 forced solely by Greenland. The total water mass losses required to achieve these targets are 7.24×10^5 Gt and 1.81×10^6 Gt, respectively (Table 1). Of this mass, 2.58×10^4 Gt (less than 4% of the total for 2 m SLR) will be lost as SMB by 2100, which we estimated by integrating present-day values of mass loss forward at present-day rates of change (*15*), with present-day SMB estimated at 30% of total present-day rate of mass loss (*5*). Because future SMB is highly uncertain, we also scaled total SMB losses up by a factor of 10 to investigate the effect of uncertainty in SMB. Adjusting total mass losses for SMB contributions yields the mass to be discharged through marine-based outlets (Table 1). Even when scaled up by an order of magnitude, SMB is a very small fraction of the total loss required to produce the targeted SLR. Thus, even large uncertainties in future SMB have little influence on this calculation.

Rapid, dynamically unstable discharge of ice through calving is restricted to glaciers with beds based below sea level. We identified and calculated the aggregate cross-sectional area of Greenland's marine-terminating outlet glaciers by using surface and bed topography (*16*) and measured ice velocities (*5*) to identify all potential pathways for rapid discharge, including channels presently flowing rapidly as well as potentially unstable channels (Fig. 1 and table S1). Cross-sectional areas (gates) for each outlet were calculated at the point of greatest lateral constriction by bedrock in the glacier's marine-based reach. Ice stream widths in Antarctica can vary in time, but for Greenland outlet glaciers cross-sectional areas are constrained almost entirely by bedrock topography. Of the 290 km^2 total aggregate gate cross-sectional area, we identified 170 km^2 as the aggregate marine-based gate area where drainage to the ocean is not blocked by near-coastal sills standing above present-day sea level. All dynamic discharge (Table 2) must pass through these gates by 2100 to meet 2- to 5-m SLR targets. We considered four scenarios: velocities were calculated for both the "marine-based" gate (170 km^2) and the "total aggregate" gate (290 km^2) given both projected SMB and 10× inflated SMB losses. We then considered whether those velocities are realistic.

Coarseness of the digital elevation models (DEMs) used for surface and bed topography (*16*) led to uncertainties in the calculated gate areas, which may be substantial but cannot be evaluated directly. We accounted for a potential underestimate of gate area with a calculation using the total aggregate gate area. The total aggregate area exceeds the more relevant marine-based gate area by 70%. Uncertainties arising from the DEM more likely conceal small unresolved channels than large ones, so the actual gate areas may be smaller than we calculate (thus yielding higher velocities).

The present-day average velocity of all Greenland outlet glaciers is 0.56 km/year when weighted by drainage basin area or 1.23 km/year when weighted by gate cross-sectional area. The two weighted averages are different because gate cross-sectional area does not scale with drainage basin area. Average (present day to 2100) outlet glacier speeds required to meet 2- and 5-m SLR targets

Table 1. Fluxes and discharges for SLR targets. Q indicates total discharge to 2100 (Gt); q, Q converted to ice flux rate, total to 2100 (km^3/year); Q_1, total dynamic discharge less SMB to 2100 (Gt); q_1, Q_1 converted to ice flux rate, total dynamic flux less SMB to 2100 (km^3/year); Q_2, total dynamic discharge less 10× SMB to 2100 (Gt); and q_2, Q_2 converted to ice flux rate, total dynamic flux less 10× SMB to 2100 (km^3/year).

SLR target	SLR mm/year	Q	q	Q_1	q_1	Q_2	q_2
2 m	21.5	724,000	8,650	698,164	8,341	652,464	7,795
5 m	53.8	1,810,000	21,625	1,784,165	21,317	1,738,464	20,770

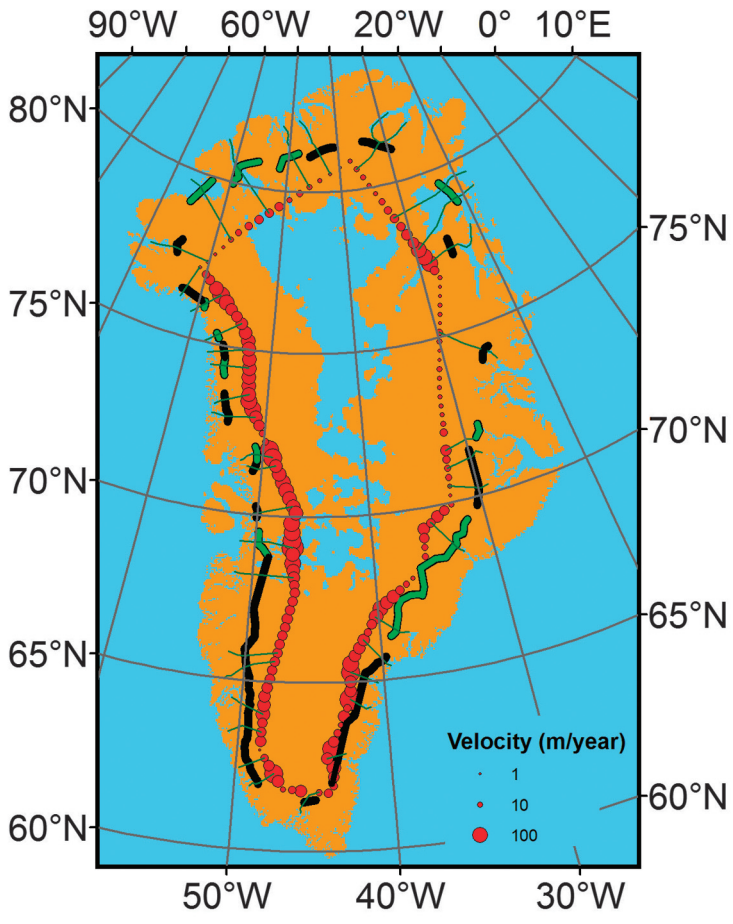

Fig. 1. Map showing Greenland and outlet glacier gates; marine-based gates are shown as dark green and nonmarine as black. Regions below sea level are colored blue. Ice velocities at ~2000 m elevation from (*21*) shown by red dots.

Table 2. Required velocities of Greenland gates for SLR targets.

SLR target	Present-day marine-based gates (km/year) 1× SMB	All present-day discharge gates (km/year) 1× SMB	Present-day marine-based gates (km/year) 10× SMB	All present-day discharge gates (km/year) 10× SMB
2 m	49	28.7	45.8	26.8
5 m	125	73.4	122	71.5

range from 26.8 km/year to 125 km/year, depending on the scenario considered [Table 2 and supporting online material (SOM)]. These velocities must be achieved immediately on all outlets considered and held at that level until 2100. Delays in the onset of rapid motion increase the required velocity further (fig. S1).

The scenario velocities far exceed the fastest motion exhibited by any Greenland outlet glacier. For example, the near-doubling of ice discharge from Jakobshavn Glacier in 2004–2005 was associated with an acceleration to 12.6 km/year (*7*). Similarly, a temporary 80% increase in the speed near the terminus of Kangerdlugssuaq produced a velocity of 14.6 km/year (*6*). A comparison of calculated (Table 2) and observed (1.23 km/year) average velocities shows that calculated values for a 2-m SLR exceed observations by a factor of 22 when considering all gates and inflated SMB and by a factor of 40 for the marine gates without inflated SMB, which we consider to be the more likely scenario. With the exception of discharge through all gates at inflated SMB (26.8 km/year), none of the velocity magnitudes shown in Table 2 has ever been observed anywhere, even over short time periods. The highest observed velocities have occurred at surging glaciers, including circa (ca.) 70 m/day (25.5 km/year) at Variegated Glacier (*17*) and 105 m/day (38.3 km/year) at Medvezhiy Glacier (*18*), but were held only for brief periods (hours to days). Although no physical proof is offered that the velocities given in Table 2 cannot be reached or maintained over century time scales, such behavior lies far beyond the range of observations and at the least should not be adopted as a central working hypothesis.

Calculations are made only for Greenland because Greenland's outlet glaciers are well constrained by bed topography, which (despite the uncertainties mentioned) is well known in comparison to much of the Antarctic Ice Sheet and the Antarctic Peninsula and virtually all of the marine-terminating glaciers and ice caps (GIC) exclusive of Greenland and Antarctica. In order to estimate how these constraints influence projections of total SLR to 2100, we calculated a zero-order range of eustatic SLR from all land ice sources. Because marine-grounded channels are not well defined in many other locations, we made approximations and scaling arguments to arrive at a range of values for total eustatic SLR and, including reasonable projections of steric SLR, a range of estimates of total SLR to 2100.

Table 3. SLR projections based on kinematic scenarios. Thermal expansion numbers are from (*22*).

	SLR equivalent (mm)		
	Low 1	Low 2	High 1
Greenland			
Dynamics	93	93	467
SMB	71	71	71
Greenland total	165	165	538
Antarctica			
PIG/Thwaites dynamics	108		394
Lambert/Amery dynamics	16		158
Antarctic Peninsula dynamics	12		59
SMB	10		10
Antarctica total	146	128	619
Glaciers/ice caps			
Dynamics	94		471
SMB	80		80
GIC total	174	240	551
Thermal expansion	300	300	300
Total SLR to 2100	785	833	2008

Most of the marine-based ice in West Antarctica is held behind the Ross and Filchner-Ronne ice shelves, which we consider unlikely to be removed by climate or oceanographic processes within the next century [e.g., (*19*)]. The Amundson Coast basin [including Pine Island Glacier (PIG) and Thwaites Glacier], however, is not confined by large ice shelves and contains about 1.5 m sea level equivalent (5.43×10^5 Gt) (*20*). The aggregate cross-sectional gate area of PIG and Thwaites Glacier is ca. 120 km^2 (*20*). The average velocity in this region is 2 km/year (table S2), higher than the average velocity of all Antarctic ice streams [0.65 km/year (*19*)]. An average (present day to 2100) velocity of 53.6 km/year is required to discharge 1.5 m sea-level equivalent through the PIG and Thwaites glacier gates by 2100, again far greater than any observed glacier velocity.

We present three scenarios by combining likely projection methods that we believe roughly bracket the range of potential near-future SLR outcomes (SOM). These are not true limiting cases but give a good sense of the potential variability of total SLR due to dynamic discharge effects.

SLR scenario Low 1 represents a low-range estimate based on specific adjustments to dynamic discharge in certain potentially vulnerable areas. We assumed a doubling of outlet glacier velocities in Greenland and PIG/Thwaites within the first decade and no change from present-day discharge values at Lambert/Amery. SMB for Greenland, the Antarctic Peninsula, and GIC was accelerated at present-day rates of SMB change, and, lacking more directly applicable constraints, dynamic discharge for the Antarctic Peninsula and GIC was calculated by scaling dynamic discharge to SMB by using the ratio of 1.31 as computed for Greenland (SOM). The net result, including thermal expansion, is 785 mm by 2100 (Table 3).

A second low-range scenario (Low 2) shows the effect of varying our assumptions; for this, we simply integrated presently observed rates of change forward in time. We calculated Greenland's contribution as for Low 1 but accelerated the present-day net discharge for Antarctica (East/West/Antarctic Peninsula) forward at the present-day rate of change given by (*19*). The GIC contribution was also calculated by accelerating the present-day net discharge at the current rate of change, with values from (*15*). The net result, including thermal expansion, is 833 mm by 2100 (Table 3).

SLR scenario High 1 combines all eustatic sources taken at high but reasonable values. No firm highest possible value can be determined for SMB or dynamics; the values chosen represent judged upper limits of likely behavior on the century time scale. Greenland SMB was accelerated at present-day rates of change, but dynamic discharge was calculated by accelerating outlet glacier velocities by an order of magnitude in the first decade. In Antarctica, PIG/Thwaites was accelerated from present-day net discharge (*19*) in the first decade and held thereafter to the highest outlet glacier velocity observed anywhere [14.6 km/year (*6*)], and Lambert/Amery was accelerated from present-day net discharge (*19*) in the first decade by an order of magnitude and held thereafter. Antarctic Peninsula and GIC were calculated by scaling dynamic discharge at the dynamics-to-SMB ratio computed for Greenland; this ratio is larger (6.42) than in case Low 1 because Greenland's dynamic discharge is larger. The net result, including thermal expansion, is 2008 mm by 2100 (Table 3).

On the basis of calculations presented here, we suggest that an improved estimate of the range of SLR to 2100 including increased ice dynamics lies between 0.8 and 2.0 m. We emphasize that assumptions made to arrive here contain substantial uncertainties, and many other scenarios and combinations of contributions could be considered. However, the net eustatic SLR from other combinations explored fell within the range given in Table 3. Hence, these values give a context and starting point for refinements in SLR forecasts on the basis of clearly defined assumptions and offer a more plausible range of estimates than those neglecting the dominant ice dynamics term. Certain potentially significant sinks and sources of SLR, such as terrestrial water storage, are still absent altogether. Among the uncertainties explored, the potential for dynamic response from GIC is comparable in magnitude to dynamic response from Greenland or Antarctica but is exceptionally poorly constrained by basic observations. Without better knowledge of the number, size, and catchment areas of marine-based outlet glaciers in the GIC category, improvements on the estimates made here will be very difficult.

References and Notes

1. S. O'Neel, W. T. Pfeffer, *Geophys. Res. Lett.* **34**, L22502 (2007).
2. M. F. Meier, A. Post, *J. Geophys. Res.* **92**, 9051 (1987).
3. M. Meier *et al.*, *J. Geophys. Res.* **99**, 15219 (1994).
4. B. Kamb *et al.*, *J. Geophys. Res.* **99**, 15231 (1994).
5. E. Rignot, P. Kanagaratnam, *Science* **311**, 986 (2006).
6. I. M. Howat, I. Joughin, T. A. Scambos, *Science* **315**, 1559 (2007); published online 7 February 2007 (10.1126/science.1138478).
7. I. Joughin, W. Abdalati, M. Fahnestock, *Nature* **432**, 608 (2004).
8. IPCC, *Climate Change 2007: The Physical Science Basis. Contribution of Working Group I to the Fourth Assessment Report of the Intergovernmental Panel on Climate Change,* S. Solomon *et al.*, Eds. (Cambridge Univ. Press, Cambridge, 2007).

9. B. L. Otto-Bliesner *et al.*, *Science* **311**, 1751 (2006).
10. J. T. Overpeck *et al.*, *Science* **311**, 1747 (2006).
11. J. Hansen, *Environ. Res. Lett.* **2**, 024002 (2007).
12. J. Hansen *et al.*, *Philos. Trans. R. Soc. London Ser. A* **365**, 1925 (2007).
13. J. Mount, R. Twiss, *San Francisco Estuary Watershed Sci.* **3**, 1 (2005).
14. E. Bard *et al.*, *Nature* **382**, 241 (1996).
15. M. F. Meier *et al.*, *Science* **317**, 1064 (2007); published online 18 July 2007 (10.1126/science.1143906).
16. J. L. Bamber, R. L. Layberry, S. Gogineni, *J. Geophys. Res.* **106**, 33773 (2001).
17. B. Kamb *et al.*, *Science* **227**, 469 (1985).
18. E. R. Hope, "English translation T409R," Defense Research Board, Ottawa, Canada, 1963 [translation from L. D. Dolgushin, S. A. Yevteyev, A. N. Krenke, K. P. Rototayev, N. M. Svatkov, *Priroda* **11**, 84 (1963)].
19. E. Rignot *et al.*, *Nat. Geosci.* **1**, 106 (2008).
20. E. Rignot, personal communication (2007).
21. R. Thomas *et al.*, *Science* **289**, 426 (2000).
22. G. A. Meehl *et al.*, in (*8*).

23. This work was supported by NSF grants OPP-0327345 and OPP-0622351 and a University of Colorado Faculty Fellowship (W.T.P.), NSF grants OPP-0612506 and OPP-0454789 (J.T.H.), and the Greens Foundation at Scripps Institution of Oceanography (S.O.). E. Rignot generously supplied Greenland surface velocity data.

Supporting Online Material

www.sciencemag.org/cgi/content/full/321/5894/1340/DC1
Materials and Methods
Fig. S1
Tables S1 and S2
References

14 April 2008; accepted 18 July 2008
10.1126/science.1159099

Apobec3 Encodes *Rfv3*, a Gene Influencing Neutralizing Antibody Control of Retrovirus Infection

Mario L. Santiago,[1] Mauricio Montano,[1]* Robert Benitez,[1]* Ronald J. Messer,[2] Wes Yonemoto,[1] Bruce Chesebro,[2] Kim J. Hasenkrug,[2]† Warner C. Greene[1,3,4]†

Recovery from Friend virus 3 (*Rfv3*) is a single autosomal gene encoding a resistance trait that influences retroviral neutralizing antibody responses and viremia. Despite extensive research for 30 years, the molecular identity of *Rfv3* has remained elusive. Here, we demonstrate that *Rfv3* is encoded by *Apobec3*. *Apobec3* maps to the same chromosome region as *Rfv3* and has broad inhibitory activity against retroviruses, including HIV. Not only did genetic inactivation of *Apobec3* convert *Rfv3*-resistant mice to a susceptible phenotype, but *Apobec3* was also found to be naturally disabled by aberrant messenger RNA splicing in *Rfv3*-susceptible strains. The link between *Apobec3* and neutralizing antibody responses highlights an *Apobec3*-dependent mechanism of host protection that might extend to HIV and other human retroviral infections.

The study of viral resistance factors has provided important insights into the evolutionary strategies of defense used by mammalian hosts (*1*–*5*). Recovery from Friend virus (FV) gene 3 (*Rfv3*) was first identified as a resistance trait in 1978 (*6*, *7*), and later genetic studies showed that the phenotypes of decreased viremia and FV-specific neutralizing antibody responses segregated as a single gene (*8*). Because the generation of neutralizing antibodies is critical for recovery from FV infection (*1*, *9*) and a desired but often unrealized outcome in various retroviral infections, including HIV-1, we have focused our efforts on identifying the gene encoding *Rfv3*. The *Rfv3* locus maps to a 0.83-centimorgan region of chromosome 15 (fig. S1A) (*10*–*12*), which contains at least 61 annotated genes (table S1), one of which is murine *Apobec3* (*mA3*), a member of a family of deoxycytidine deaminases with antiretroviral and antiretroelement activity [as reviewed in (*13*)]. This fact, along with the presence of substantial polymorphism in *mA3* (table S1), led us to consider *mA3* as a prime candidate for *Rfv3*.

Because *Rfv3* has no described in vitro phenotype, our investigation required the generation of *mA3*-deficient mice (*14*). First, an inactivated *mA3* gene (fig. S1B) was introduced into the $Rfv3^{r/r}$ C57BL/6 (B6) background to test its ability to act as a defective *Rfv3* allele in matings with $Rfv3^{s/s}$ mice (Table 1). Because the *Rfv3* resistance trait is dominant over susceptibility (*7*), $Rfv3^{r/s}$ F_1 offspring should control viremia and mount effective neutralizing antibody responses. Conversely, if *mA3* encodes *Rfv3*, then the gene from a $mA3^{-/-}$ parent will be null, and the resultant F_1 offspring with an $Rfv3^{-/s}$ genotype are predicted to exhibit higher levels of viremia and weaker neutralizing antibody responses. To test this possibility, B6 x BALB/c F_1 offspring were infected with FV and plasma viremia levels were measured. At 7 days post infection (dpi), the F_1 mice containing an inactivated *mA3* gene exhibited levels of viremia 15 times as high as their congenic partners carrying the wild-type *mA3* allele (Fig. 1A). These high viral loads in $mA3^{-}$ F_1 mice were comparable to FV levels found in fully susceptible $Rfv3^{s/s}$ BALB/c parental mice. Thus, *mA3* is a restriction factor contributing to the

[1]Gladstone Institute of Virology and Immunology, San Francisco, CA 94158, USA. [2]Laboratory of Persistent Viral Diseases, Rocky Mountain Laboratories, National Institute of Allergy and Infectious Diseases, Hamilton, MT 59840, USA. [3]Department of Medicine, University of California, San Francisco, CA 94143–1230, USA. [4]Department of Microbiology and Immunology, University of California, San Francisco, CA 94143–1230, USA.

*These authors contributed equally to this work.
†To whom correspondence should be addressed. E-mail: khasenkrug@nih.gov (K.J.H.); wgreene@gladstone.ucsf.edu (W.C.G.)

Table 1. FV infection characteristics of various mouse strains used in this study.

Type	Strain	General FV susceptibility	Viremia	*Rfv3*	Neutralizing antibody	*H-2**	Cell-mediated immunity	*Fv2*†	Splenomegaly induction
Wild-type	C57BL/6 (B6)	Resistant	Resistant	*r/r*	High	*b/b*	High	*r/r*	No
	BALB/c	Susceptible	Chronic	*s/s*	Low	*d/d*	Very low	*s/s*	Yes
	A.BY	Susceptible	Chronic	*s/s*	Low	*b/b*	High	*s/s*	Yes
	129/Ola‡	Resistant	Resistant	*r/r*	High	*b/b*	High	*r/r*	No
F_1 hybrids	B6 x BALB/c	Susceptible	Acute	*r/s*	High	*b/d*	Low	*r/s*	Yes
	B6 x A.BY	Susceptible	Acute	*r/s*	High	*b/b*	High	*r/s*	Yes

**H-2* is the murine major histocompatibility complex that dictates cell-mediated immunity against FV (*5*, *15*). †*Fv2* is a dominant FV susceptibility gene that facilitates splenomegaly induction through aberrant signaling in erythroblasts (*4*). ‡FV susceptibility data on 129/Ola were based on results from this study (Fig. 2C) (*14*). The cell-mediated immune response of this strain was inferred from its *H-2* haplotype.